Comb coherence-transfer and cavity ring-down saturation spectroscopy around 1.65 μm: kHz-accurate frequencies of transitions in the 2ν3 band of 12CH4

Ondrej Votava, Samir Kassi, Alain Campargue, Daniele Romanini

PCCP

ARTICLE TYPE

Cite this: DOI: 00.0000/xxxxxxxxxx

Comb coherence-transfer and cavity ring-down saturation spectroscopy around 1.65 μm: kHz-accurate frequencies of transitions in the $2\nu_3$ band of $^{12}CH_4$

Ondrej Votava,[b] Samir Kassi,[a] Alain Campargue,[a] and Daniele Romanini*[a]

Received Date
Accepted Date

DOI: 00.0000/xxxxxxxxxx

Comb Coherence Transfer (CCT) uses a feed-forward frequency correction to transfer the optical phase of a frequency comb to the beam of a free-running diode laser. This allows to amplify by 50 dB a selected comb tooth while adding agile and accurate frequency tuning. In the present work, SI-traceable frequency calibration and comb tooth narrowing down to 20 kHz is additionally provided by comb frequency locking to an ultrastable optical frequency reference distributed from Paris to Grenoble through the RENATER optical fiber network [Lisdat *et al., Nature Communications*, 2016, **7**, 12443]. We apply this CCT broadly tunable source for saturated cavity ring-down spectroscopy of ro-vibrational R0 to R10 multiplets in the $2\nu_3$ band of $^{12}CH_4$ (from 6015 to 6115 cm^{-1}). Indeed, efficient cavity injection with large intra-cavity power build-up induces saturation of the ro-vibrational transitions at low pressure and Doppler–free Lamb dips are observed with high signal/noise. kHz-accurate transition frequencies are derived improving by three orders of magnitude previous values from spectra in the Doppler regime, which are strongly affected by line blending. While previous saturation spectroscopy investigations addressed specific $2\nu_3$ multiplets (R6 or R9), the CCT approach allowed for a rapid coverage of the entire R0-R10 series. Measured transition frequencies are compared with experimental and theoretical line lists available in the literature.

1 Comb coherence transfer

Introduction of the optical frequency comb (OFC), featuring regularly spaced teeth with absolutely defined frequencies over a wide spectral range, has brought fundamentally new capabilities to high resolution spectroscopy, providing means for absolute frequency calibration in the optical range that is directly traceable (SI-traceable) to the primary standards of time and frequency. By measuring the offset frequency between a tunable probe laser source used for spectroscopy and the nearest frequency comb tooth *via* beat-note detection, absolute frequency of the probe laser is determined with an unprecedented accuracy and simplicity. Besides this already well appreciated fact, other features of this tool are emerging and being utilized by the spectroscopic community. One of them is the extremely low phase noise of the individual teeth observed in a well stabilized frequency comb. Indeed, fractional frequency uncertainty of 10^{-17} in 1 s interval has been achieved even in commercial systems, limited by the accuracy of the primary Cs atomic clock accuracy.[1,2]

With this improved absolute frequency calibration, molecular linewidth become the primary limitation in line position measurements. At low pressures, when collision broadening is negligible, Doppler broadening is usually the limiting factor, leading to a typical room temperature linewidth of hundreds of MHz in the near-IR and visible ranges for most small polyatomic molecules. While line centers have been determined with uncertainty below $\delta\nu < 10$ kHz for isolated spectral lines,[3–5] the situation is much worse in cases when multiple spectral lines are overlapping within their Doppler widths, necessitating multi-line fits. Line uncertainties of tens of MHz are common in such situations.[6] This is often the case for molecules exhibiting fine and hyper-fine splittings or complex vibration-rotation interactions. One such case is the vibration-rotation spectra of spherical top molecules where the rotational $2J+1$ degeneracy is lifted by Coriolis and centrifugal interactions leading to closely spaced multiplets in the observed spectra.

To reach the full potential in absolute frequency measurements offered by OFC based calibration, it is therefore important to circumvent the Doppler broadening. One general approach is sample cooling, but as the Doppler width is proportional to the square

[a] *Université Grenoble Alpes, CNRS, LIPhy, 38000 Grenoble, France. Fax: (33)(0)476514544; Tel: (33)(0)476514767; E-mail: daniel.romanini@univ-grenoble-alpes.fr*

[b] *J. Heyroskyt' Institute of Physical Chemistry, ASCR, Dolejkova 3, Prague 8, Czech Republic.*

root of temperature, only moderate linewidth reduction can be practically achieved.[7–9] Using supersonic jets or collisional cooling for reaching temperature of a few Kelvins is more effective but still leads to a reduction of Doppler widths by at most a factor ten. An additional problem is that cooling also depopulates rotations and vibrations and does not allow accessing most molecular transitions observed at room temperature.

An alternative approach is provided by saturation spectroscopy, which offers virtually Doppler-free spectra. This technique utilizes two counter-propagating light beams passing through the sample gas, with enough intensity to deplete the lower state population in the interrogated transition. Reduced absorption is then observed when both beams interact with the same velocity group of the absorbing molecules, which happens when the laser frequency is tuned to the center of the Doppler broadened line profile, where molecules with close to zero velocity projection along the laser beam axis absorb radiation from both directions.[10] Narrow, inverted absorption dips (Lamb dips, in honor of W. E. Lamb, who first described the effect[11]) are thus observed in the centers of the Doppler-broadened spectral lines even in room temperature samples. Spectral width of those dips is only limited by lifetime effects (such as the natural lifetime of the upper state, collision broadening and/or transit time) and by power broadening.

Intensities required to reach the saturation regime are inversely proportional to the Einstein coefficient for absorption, B_{12} and thus to $\nu^3 A_{12}$, where A_{12} is the Einstein coefficient for spontaneous emission and ν is the transition frequency. Saturation intensity varies over many orders of magnitude depending on the specific molecular transition. Indeed, the dipole allowed electronic transitions were the first to be studied by the saturation techniques due to their high transition probabilities,[12,13] with mW laser intensities corresponding to fluxes below 100 mW/cm^2 being sufficient to observe the effect. Vibrational transitions in general have lower transition probabilities and thus higher saturation light intensities are required. By a lucky coincidence between methane P(7) transition of the ν_3 fundamental band and the He-Ne laser infrared emission at 3.39 μm, saturation spectroscopy could be applied to this rovibrational line since early stages of laser development.[14] The effective light intensity had to be increased to 2.5 W/cm^2 by using a laser intracavity arrangement. Experiments targeting the much weaker combination and overtone bands in the near-IR range require still higher saturation laser intensities. As an example, the first overtone of the ν_3 vibration of methane near 1.6 μm has the $B_{12} \sim 80$ times weaker, compared to the corresponding fundamental band, requiring laser fluxes on the order of 100 W/cm^2 to achieve saturation.

Such light intensities exceed significantly the output power of most available lasers in the spectral range of interest. Specifically, tunable diode lasers widely used as practical spectroscopic sources in the near-IR have a typical output below 100 mW. With beam diameter of 1 mm, giving a reasonable compromise between desired power density and small transit time broadening, achievable power densities are below 10 W/cm^2, insufficient to reach the saturation regime. Power build-up in optical resonators provides a practical tool to increase light intensity in the absorption volume. Inside an optical resonator formed by two mirrors with reflectivity R, light intensity may reach $I = \alpha F I_0$, where $F \simeq \pi/(1-R)$ is the finesse and $\alpha < 1$ represents the coupling efficiency that depends on the mirror transmission T, the mode matching between the cavity and laser beam, and the effective duration of cavity injection (proportional to laser-cavity resonance duration and to the ratio of cavity linewidth over laser linewidth). With practical resonator finesse $F \sim 10^5$, circulating powers of ~ 100 W are possible even with 1 mW input power, assuming high coupling efficiency $\alpha \sim 1$ is achieved. Saturation spectroscopy of the weak vibrational overtone and combination bands has been first demonstrated by Labachelerie and coworkers[15] using a modest finesse ($F \approx 200$) build-up cavity and its capabilities for sub-MHz absolute frequency calibration in combination with an OFC has been first reported by Ishibashi and coworkers.[16] However, only recent advances in laser technology and introduction of high sensitivity detection techniques, such as cavity ring-down spectroscopy (CRDS), make saturation spectroscopy attractive for a wide range of problems in high precision molecular spectroscopy and optical metrology.[6,17–27]

It is important to underline that application of high-finesse optical resonators for saturation spectroscopy demands laser radiation of high spectral purity. A first reason is that Lamb dips are spectrally narrow: Lorentzian widths of less than 500 kHz are typically observed. This poses a demand on the laser linewidth on the timescale of spectrum acquisition and averaging, typically seconds to minutes. A second reason is the efficient coupling to the optical resonator, requiring the short term laser linewidth to be close to the cavity mode width (on the cavity buildup timescale). For a typical case of a build-up cavity with free spectral range $\Delta f = 300$ MHz and finesse $F = 10^5$, the mode FWHM (full width at half-maximum) is 3 kHz. In contrast, typical tunable near infrared laser systems such as ECDLs (external cavity diode laser) or DFB DLs (distributed feed-back diode laser), exhibit an emission linewidth on the order of 100 kHz or 1 MHz, respectively. Under those conditions, only a fraction of the laser light is coupled to the resonator, and injection is noisy,[28] hindering the build-up advantage.

One strategy to address both those issues is to lock the probe laser to the CRDS/build-up optical resonator by a feedback loop. Frequency tuning is then usually achieved by changing the reference resonator length. Short term frequency stability is then limited by resonator mechanical vibrations and by the tightness of the feedback servo loop. The long term frequency stability is limited by thermal and/or pressure induced drift of the cavity optical length unless it is stabilized by locking *via* another feedback loop to an absolute frequency reference laser. Such approaches are quite complex to implement but were successfully exploited by a few research groups for high precision saturation spectroscopy in the near infrared range.[18,20,22,24] In a related scheme developed in our group, ultra narrow and stable emission from a DFB DL is obtained thanks to optical feed-back from a low drift isolated cavity and is the basis for a tunable source for CRDS saturation spectroscopy.[6] Beating with an OFC is still used for long term absolute frequency calibration.

The CCT (comb coherence transfer) approach that we recently introduced,[29] provides an alternative for achieving stable and

narrow probe laser emission and efficient injection of a high–finesse cavity, with the added value of a broad spectral coverage and no need for a highly stable reference cavity. CCT is based on direct coherence transfer from a selected OFC tooth as a stable low phase noise master laser[1] of absolutely known frequency to a DFB DL as a broadly tunable slave laser. The novelty of CCT is that it does not rely on a phase lock loop, a standard method but hardly exploitable with a MHz–linewidth DFB DL. Instead, CCT exploits a high-bandwidth feed-forward control for direct frequency correction of the probe laser radiation.[17,30] This lifts all stringent requirements on long term mechanical stability of the build-up/CRDS resonator. As the obtained source linewidth is in the kHz range, close to the cavity mode width, the resulting high coupling efficiency yields strong and reproducible intracavity power build-up.

In addition to narrowing the probe laser linewidth, CCT allows broadband frequency coverage with a highly repeatable frequency axis. Fine and agile tuning of the probe laser is achieved by varying the RF frequency offset between the selected OFC tooth and the phase-corrected probe. Then, switching of the DFB DL between consecutive OFC teeth allows for gap-free tuning across the full tuning range of the DL laser.[17,30] Even wider coverage is easily obtained by switching several telecom fibered DFB DLs in the same setup, with minimal adjustments. As a demonstration of the efficiency and robustness of the CCT technique we present a first broadband application by harvesting an extensive set of high quality Lamb dip profiles for the $2\nu_3$ overtone band of $^{12}CH_4$, across the range spanned by 5 fibered DFB DLs.

As a further improvement relative to our previous demonstration of the feasibility of saturation spectroscopy,[30] our OFC is optically locked to an ultrastable optical frequency reference generated in the SYRTE laboratory in Paris and delivered to our laboratory in Grenoble through the RENATER telecommunication fiber network.[31] This provides SI-traceable accuracy and additional strong reduction of the OFC teeth linewidth.

2 Experimental setup

The principle of operation of the CCT technique is schematized in figure 1 and was previously introduced in Gotti *et al.*[17]. Telecom fibered distributed feedback diode lasers (DL) are used as sources of tunable probe radiation. We have used five DLs (butterfly packaged, by NEL) to cover a spectral region limited at long wavelengths by the working range of InGaAs photodiodes, at short wavelengths by the falling strength of methane transitions. A small fraction of the DL output (10%) is mixed with the comb spectrum by using a 50/50 fiber combiner and detected with a home-made fast balanced detector, which delivers the beat notes of the DL with the neighboring comb teeth. The lowest beat note (a few MHz wide) resulting from interference with the closest comb mode is separated by a low pass filter. This signal carries information on the instantaneous frequency difference between the (stable) OFC mode and the (fluctuating) DL. The signal is amplified and injected into a radio frequency (RF) single-side-band (SSB) modulator which allows adding a frequency offset from a computer-controlled synthesizer. This RF shifted beat note is then injected into the RF input of an optical SSB generator (a telecom dual Mach-Zehnder modulator, MZM), whose optical input port receives 90% of the DL power. At the MZM optical output, the selected side-band is the one with subtracted comb-DL relative frequency fluctuations. This side-band is an almost perfect phase clone of the comb mode, shifted by the tunable RF offset.[17,30]

The selected side-band at the output of the optical SSB carries from 5 to 10% of the input power, typically 1-2 mW. In order to enhance signal/noise of ring-down decay signals at cavity output and to also achieve stronger saturation levels of the molecular transitions, we used a semiconductor fiber boost optical amplifier (BOA, from Thorlabs) with a gain of about 15. The latter is followed by an acousto-optic switch which allows to initiate ring-downs in the high finesse optical cavity.

In order to avoid accumulation of wall out-gassing impurities in the sample (mostly water vapor), a continuous sample flow was used. To achieve microbar sample pressure we used a capillary at the cavity input and a proportional electrovalve between cavity output and the vacuum pump. A 10 Torr Baratron pressure gauge was used to control the sample pressure *via* a computer program acting on the electrovalve. Given the rather high cavity finesse (dropping from $F = 6.1\times10^4$ to $F = 3.7\times10^4$ when going from 6015 to 6115 cm^{-1}), the strength of $^{12}CH_4$ transitions at the lowest pressure that we could obtain ($\sim 3\,\mu$bars) demanded a diluted methane sample. Thus, even though we succeeded in recording some of the spectra using pure methane, the majority of presented data were obtained with a mixture of 5% methane in argon.

Frequency referencing to a SI-traceable source

For more details of operation and performance of this setup, we redirect the reader to our previous work.[17] One change we implemented for the present measurements is using a fibered acousto-optic modulator (AOM) as a fast optical switch to interrupt cavity injection, allowing for a more complete extinction of the source (compared to previous switch-off of the RF input of the SSB generator). Since the AOM adds a frequency shift equal to that of its driving RF power, this is provided by an amplified direct digital synthesizer (DDS) referenced to an accurate 10 MHz Rb clock standard (long-term GPS stabilized). Likewise, the tuning RF offset for the MZM is provided by a synthesizer referenced to the same Rb-GPS clock.

Moreover, as a major improvement relative to our previous work, we optically locked our frequency comb (Menlo systems model FC-1500-250-WG) to a long-haul 194400009500000(1)Hz narrow and ultra stable frequency reference provided by the REFIMEVE network.[31] This directly SI-traceable optical reference is generated at LNE-SYRTE and transferred over about 1000 km through a dedicated and modified line of the RENATER academic fiber network (https://www.renater.fr/en/history).[31,32] The phase fluctuations along this transfer line are actively compensated from Paris to Grenoble using a chain of phase-locked optical repeaters. The development of this distributed frequency standard is underway in the frame of the REFIMEVE+ project (see Acknowledgments section).

Our OFC is stabilized by controlling the femtosecond pulse

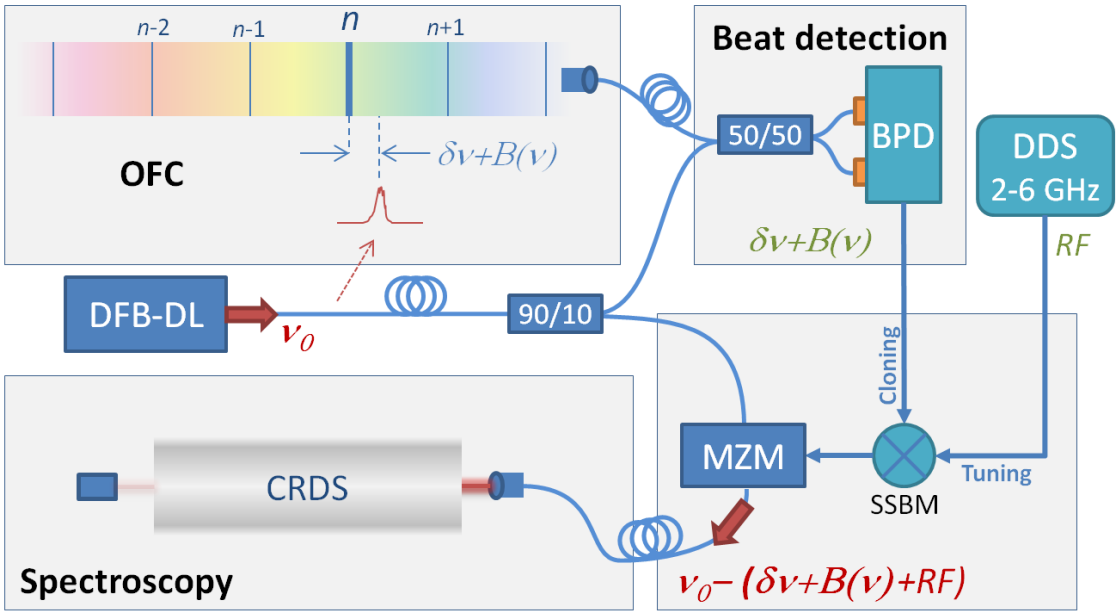

Fig. 1 Experimental fibered setup: 10% power from a distributed feed-back diode laser (DFB DL) mixed with an optical frequency comb (OFC) gives a beatnote on a balanced photodiodes (BPD). This carries the DL frequency fluctuations relative to the closest comb tooth. A single side-band modulator (SSBM) adds a tunable RF offset controlled through a direct digital synthesizer (DDS). A Mach-Zehnder modulator (MZM) acts as as an optical SSB modulator and subtracts the shifted beatnote from the rest of the DFB emission, resulting in a frequency-tunable phase clone of the OFC tooth. Less than 10% power in the single side-band result in about 10 mW available after an optical amplifier (not represented) for cavity ring-down spectroscocpy (CRDS). Also not represented are a wavemeter and the OFC locking scheme to a SI-traceable source for frequency referencing.

train repetition rate f_{rep} (corresponding to the teeth spacing in the frequency domain), monitored by a fast photodiode, and the comb frequency offset f_{co} (given by the pulses carrier–envelope slip frequency), monitored *via* a standard *f-2f* beating scheme. Both these RF-domain frequencies are usually phase-locked relative to the above mentioned Rb-GPS 10 MHz clock. Alternatively, this comb is equipped with and intracavity electro-optic modulator allowing high bandwidth control of f_{rep} for phase locking of a comb tooth to the REFIMEVE+ optical reference. This mode spacing stabilization replaces the above mentioned RF lock of f_{rep} to the Rb-GPS clock. As a result, comb frequencies become more stable on short timescales, since the optical reference short-term (<1 ms) linewidth at our laboratory is about 20 kHz (FWHM). In addition, long-term stability of the SYRTE source is also way better than for a Rb-GPS clock.

Concerning short-term fluctuations, we should remark the following. Despite the μHz stability of the 10 MHz Rb-GPS clock, when RF locking f_{rep} to this clock there is a large multiplication factor (close to 7×10^5) to reach up to optical frequencies where the comb operates. This multiplication factor applies also to the Rb clock phase noise, yielding in our case a comb mode width of about 200 kHz. Optical locking to the REFIMEVE+ source then improves our comb tooth linewidth by a factor ten. We consider short-term linewidth due to phase-frequency fluctuations on μs to ms timescales since these are the relevant timescales for the injection dynamics of a high finesse cavity.

It is obviously relevant to address the question of the Doppler frequency shift induced by the ring-down cavity length change during the recorded light decays. Indeed, repetitive cavity injections (at a rate around 400 Hz) are obtained by a tight tracking scheme based on a fine dithering of the cavity length around resonance with the laser. The dithering range is around 1 MHz giving some 20 kHz of Doppler shift during one ring-down decay time constant (<30 μs). The shift over the 3-4 decay time constants which are determinant in the fit of a decay profile is then still 10 times below the linewidth of the observed Lamb dips (>600 kHz). In the worst case, during the acquisition of a spectral point standing on the maximum slope of a dip profile, there will be a small contribution to the changing molecular saturation (mainly due to falling optical power) due to this shifting of the saturated velocity class (as discussed below, molecular population renews faster than the decay time). However this effect cancels, at the first order, given the alternating direction of the passages through resonance when averaging some 100 ring-downs per spectral point. Indeed, Doppler shifts of opposite sign are induced, with saturated velocity classes shifting alternatively towards and away from the dip center. Being these shifts a small fraction of the dip profile, the profile may be approximated by the local linear slope, from which we can assume cancellation of effects at first order upon averaging. We then see that this averaging effect combined with the symmetry of the Lamb dip profiles (as observed and discussed below) cannot result in a shift of the transition frequencies determined from fitting the dip profiles. Regarding second order effects which would survive the averaging, due to profile symmetry they would only impact its linewidth.

Spectral tuning

As previously illustrated,[17] by exploiting the standard frequency control of a DFB DL through its operating current and temperature, it is possible to obtain continuous piece-wise tuning of the CCT source limited only by the DL spectral range, typically spanning 1 THz (33 cm^{-1}). However, short–range RF tuning is sufficient here to cover each group of lines composing the $^{12}CH_4$ multiplets in the $2\nu_2$ rovibrational band (in particular those with higher rotational excitation). Thus, DL current and temperature were adjusted manually to reach the starting point for each RF frequency scan by monitoring the emitted frequency by a fiber–coupled wavemeter (High-finesse WS7-IR). The starting point was chosen based on HITRAN[33] simulations of the Doppler–broadened multiplets. Then, several scans for each group of lines were performed in order to have some statistics on the determination of transition frequencies *via* the Lamb-dip positions. In some cases, we acquired scans over several hours, which allowed us to confirm the long term stability of the measured transition frequencies (no drift was observed). In order to cover all multiplets from R0 to R10, we employed 5 fibered DFB diodes (butterfly casing, by NEL), easily interchangeable in a CCT setup.

Lamb dips detection strategy

With high intracavity power and low collisional rate (μbar pressure levels), strong saturation of $^{12}CH_4$ transitions was readily observed through markedly non-exponential ring-down decays, a well known feature of transition saturation in CRDS.[6,34] Given the difficulty of implementing a real-time fitting procedure for non-exponential decays, averaged ring-down profiles for each spectral point were saved to a file for later analysis. This was also useful for testing different saturation models after data collection. It should be underlined that each decay started from a fixed amplitude threshold triggering the interruption of cavity injection. This allowed co-adding identical decay profiles without distortion of their nonlinear behavior.

For convenience, a simple exponential fit of the decays was however used during spectral scans to visualize approximate spectral profiles, including the presence of Lamb dips. In order to identify the Lamb-dip positions, given the insufficient accuracy of line centers provided by the HITRAN database, we proceeded to fast survey scans. These used reduced averaging (20 ring-downs per step) and fine steps (0.5 MHz) to cover the central section of the Doppler profile of each line. Thanks to agile RF tuning and high ring-down acquisition rate (400 ring-downs per second, typically), such a survey scan lasted only a few minutes. Afterwards, we could set up higher resolution scans (20 kHz steps, usually) with higher averaging (100 ring-downs per step) covering small spectral windows around the detected Lamb-dip positions. Figure 2 displays a sample of scans over several multiplets, including low resolution outlines of the Doppler profiles and high resolution sections around the dips.

3 Data analysis

In this section we discuss the analysis we developed to go from the recorded (averaged) non exponential ring-down decays to the Lamb dip profiles, whose fit provides a list of accurate transition frequencies representing the main result of this work. Not less important, we will also outline our procedure leading to an estimation of systematic error bars for these transition frequencies.

Modelling the saturated ring-down decay

In all our measurements, the intracavity light decay turns out to be sufficiently slow that saturation of the molecular transitions adiabatically follows the power decay. In particular at μbar pressures the mean free path between successive molecular collisions (more than 1 cm at 1 μbar for elastic velocity-changing collisions) is much larger than the light beam waist. In our case, cavity injection is mode matched to the fundamental transverse cavity modes having a Gaussian profile with about 1 mm diameter (increasing by only 15% from cavity center to its ends). The interaction time is then given by the beam diameter divided by the average molecular speed, 630 m/s for methane at room temperature: Less than 2 μs and much shorter than the ring-down time of our cavity (which ranges from 20 to 33 μs going from longer to shorter wavelengths in the explored region).

This simplifies the physical model of intracavity saturation and decay dynamics. In particular, ballistic passage through the interaction region avoids spatial non uniformity of the saturation which could otherwise be expected considering the variable light intensity across the beam profile, and could in turn affect the cavity mode profile itself. To reinforce this point, we should notice that sample absorption is here very small, about 10^{-5} per pass for the strongest absorption lines. The instantaneous intracavity light loss rate γ can therefore be reduced to the sum of a constant cavity loss rate γ_{cav}, and a time dependent saturated sample contribution γ_s which corresponds to the instantaneous intracavity power level. In the inhomogeneous broadening regime (Doppler broadening of the absorption lines at low pressure), this last term can be written[35] as $\gamma_s = c\,\alpha(\nu)/\sqrt{1+I(t)/I_s(\nu)} = c\,\alpha_{sat}(\nu)$ where $\alpha(\nu)$ is the linear absorption coefficient composed of the molecular absorption lines, $I(t)$ is the decaying intracavity light power, $I_s(\nu)$ is the saturation power (expressed in the same units as $I(t)$), and c the speed of light. Thus, molecules with close to zero longitudinal velocity, or more precisely with Doppler shift smaller than the homogeneous broadening, interact simultaneously with the forward and backward traveling light fields inside the cavity when the optical frequency matches the transition frequency. These molecules are then more strongly saturated than other velocity classes. It is interesting to notice that, as the observed ring-downs are produced (or fitted, see below) with close to constant initial amplitude (intracavity power $I(t_0)$) across a whole spectral scan, it is actually the saturation power parameter I_s which must decrease in correspondence with a Lamb dip, given that the saturation term $I(t_0)/I_s$ must increase for zero velocity molecules.

To analyze the saturated ring-down profiles recorded when tuning across the Lamb dip features, we then apply this non-linear model (NL) which produces accurate fits as illustrated in the top of figure 3. A merit of this fit model is that it is based on physical insight and its parameters have a clearly identified physical meaning. None of the few other models we tested would provide

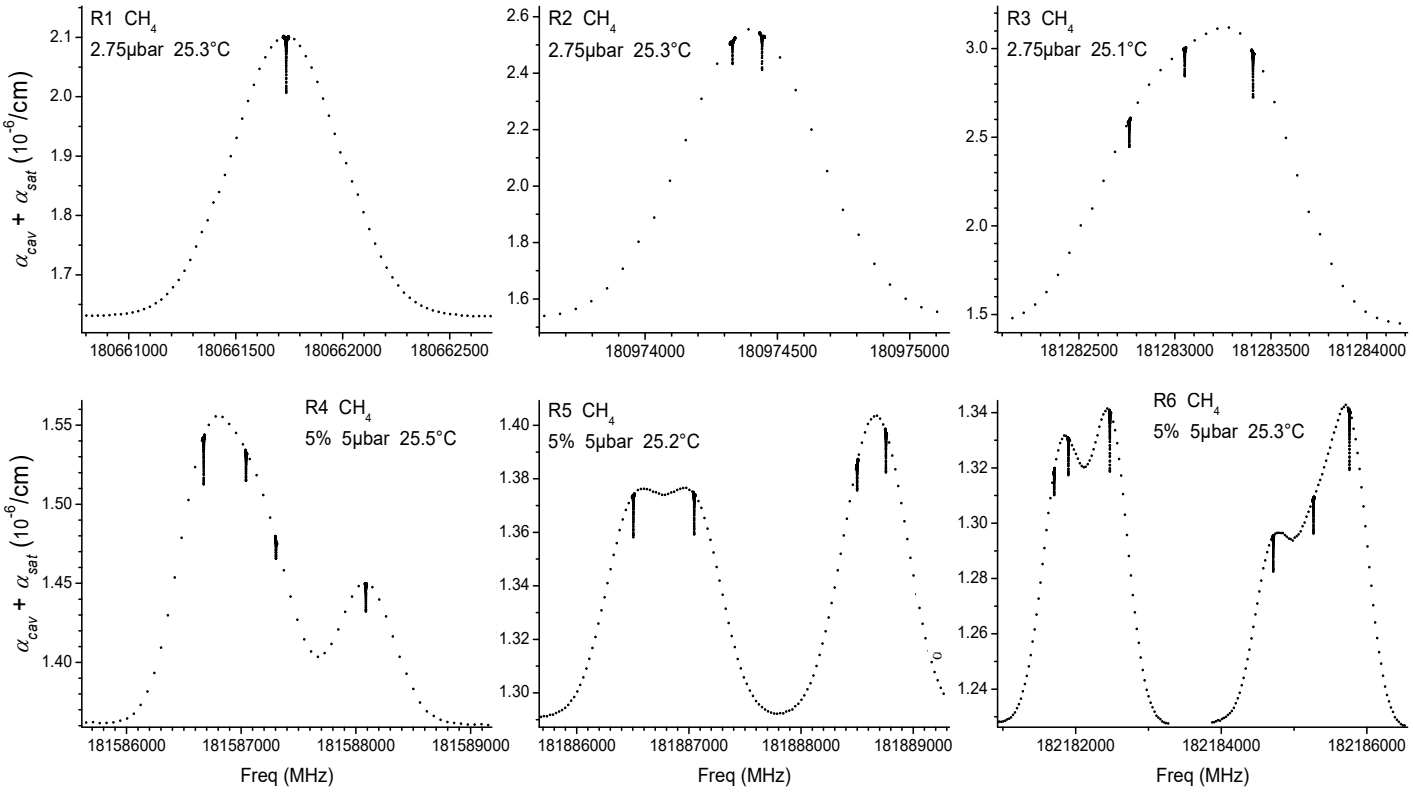

Fig. 2 CRDS spectra of some $^{12}CH_4$ $2\nu_3$ R-branch multiplets, with higher resolution scan sections around the saturation Lamb dips. Vertical scales give the total intracavity losses per unit length. The saturated sample absorption α_{sat} is on a baseline α_{cav} from cavity losses (see text).

comparably satisfactory fits, including the one proposed in Yang *et al.* [36], which in most cases have convergence problems (we implemented it using the standard Levemberg-Marquardt nonlinear fit routine). It should however be understood that even the proposed model is simplistic and should be considered mostly as a good fitting function. In fact, even though it accounts well for the evolution of the ring-down decays across the profile of a Lamb dip (as explained below), it does not work across the whole Doppler profile. In particular, good ring-down fits across the Doppler profile can be obtained only by allowing the cavity loss parameter γ_{cav} to vary, while it should clearly remain constant. There is also a non negligible and non physical dependence of fit parameters with the initial ring-down power as discussed below.

In order to explain how the ring-down fit is implemented, we reformulate the model as $I(t) = I_0 \exp[-\left(\alpha_{cav} + \alpha/\sqrt{1+I(t)/I_s}\right) ct] + b$, where we added the photodetector offset b and introduced the empty cavity absorption $\alpha_{cav} = \gamma_{cav}/c$ (even though cavity losses are localized on the mirrors, it is equivalent to consider them as uniformly distributed along the cavity length). As $I(t)$ appears in the decay function itself, the fit can be implemented iteratively: $I(t)$ is first replaced by the result of a simple exponential fit to the ring-down profile, then the resulting optimized profile is taken for $I(t)$ in the next fit iteration, and so forth until convergence. This iterative scheme converges quite robustly, i.e. even for a choice of initial parameters quite far from the right solution.

When applying this model to the recorded ring-down signals, we can still choose to start fitting the decay at a given time delay t_0 from the beginning of the ring-down recording. This allows to select an optimal saturation level for obtaining the best Lamb dip profile. The delay will be represented herein by an integer parameter PS (points skipped, 4 μs per point here) which gives t_0 as the number of digitized data points from the beginning of the ring-down decay. A seemingly more appropriate alternative would be to use an amplitude threshold to fix the starting point for the fit. Unfortunately, that introduces sizable discontinuities in the fit results when the number of data points after the threshold changes by one as the decay slope evolves across a dip profile. While the fit is everywhere excellent, with residuals below 0.01% (top of figure 3), the optimized values of the fit parameters may vary by as much as 15% as a function of PS for any given ring-down recording (see bottom panel in figure 3). This is another indication that our saturation model is too simplistic.

For a fixed PS value, the ring-downs inside the high resolution scan window around a Lamb dip are fit keeping α_{cav} and α constant (to values obtained by a full ring-down fit on the dip baseline). Indeed, these two parameters are not supposed to vary over the scan interval which covers a tiny fraction of the Doppler profile. These fits deliver the saturation power I_s, together with the initial decay amplitude I_{PS} (same as $I(t_0)$ before), and the offset b, as a function of scan frequency ν. The Lamb dip spectral profile for initial laser power I_{PS} is then given by the saturated absorption coefficients $\alpha_{sat}(\nu) = \alpha/\sqrt{1+I_{PS}/I_s(\nu)}$, where the ν dependence is through I_s as already explained. It should be added that fixing α is not only a physically meaningful approximation, it is also needed to obtain a low–noise spectral profile. Given the

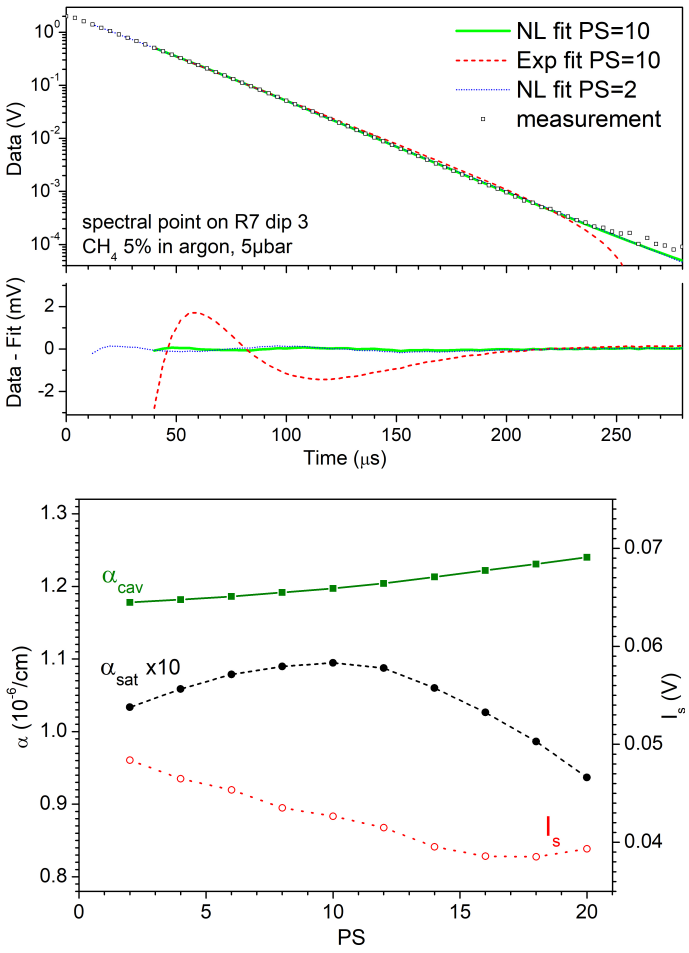

Fig. 3 Top: Typical averaged saturated ring-down decay fitted by the NL model and by a simple exponential (Exp), for a spectral data point sitting on the third R7 Lamb dip. The PS parameter indicates the number of data points skipped (4 μs/point) from the beginning of the recorded ring-down. Bottom: evolution of principal NL fit parameters as a function of PS. See text in particular for definition of saturation intensity I_s and intracavity losses per unit length α_{cav} and α_{sat}.

clear correlation between α and I_s, if both these parameters are left free the noise on the recorded ring-down profiles is amplified as it projects on the two parameters in random amounts for each spectral point, leading to a much noisier spectral profile.

Power dependence of Lamb dips

After obtaining a Lamb dip profile from fitting the recorded (and averaged) ring-down decays, a Voigt fit is applied to extract the width, the area, and especially the dip position yielding the transition frequency to high precision and accuracy. A Gaussian component in this profile would be expected to correspond to the Fourier transform of the field time profile seen by molecules traversing the Gaussian cavity mode, mostly without collisions (given the low pressure, as discussed earlier). We estimate the linewidth associated to this transit time, in the conditions of our measurements, to about 410 kHz FWHM. [10] This is definitely smaller than the measured values of around 700 kHz, even though the discrepancy is not large. On the other hand, Voigt fits of all observed Lamb dips are found to converge to an almost pure Lorentzian, with fit residuals close to the noise level. A typical case is shown in fig.4 (for optimal PS=15, as discussed below). In fact, averaging over the molecular speed distribution, with contribution to saturation decreasing as a function of speed (larger contribution for larger transit times), should result in a saturation dip profile close to Lorentzian when the transition relaxation time is about equal to the average transit time (figure 2a in Bordé *et al.* [37]). At our low sample pressure, however, this condition should not be satisfied. As elastic collisions should be the principal drive to the relaxation time, even though they have larger cross section than inelastic collisions, their typical values are far from accounting for a relaxation time as short as the transit time. In this case, the Lamb dip profile should be more peaked than Lorentzian (figure 2b in Bordé *et al.* [37]) and not compatible with a Voigt profile. It does then appear that we have a disagreement with theory, however this is a complex matter which goes beyond the scope of this work. For one thing, we have not considered the effect of power broadening which might be strongly affecting our measurements in the direction of a Lorentzian profile wider than from transit time. We note for instance that in fig.3 the saturation intensity parameter for the ring-down fit is small relative to the initial fit amplitude (even for large PS values).

We should then consider that the Voigt profile is used here as a generic adaptable function which fits well the dip profiles, as illustrated on the top panel of figure 4. A Lorentzian profile would have been as accurate most of the time, given the small or negligible Gaussian components resulting from the fits, but the additional computational cost of a Voigt fit was irrelevant. It should also be underlined that wiggles in the Voigt fit residuals, which sometimes dominate over the noise level (not the case in the figure), are never asymmetric around the line center when we choose an optimal saturation level (as discussed below). Therefore our choice of a symmetric profile function is not expected to introduce biases in the estimation of the dips positions. It turns out however, that even the presence of symmetrical fit residuals induces non negligible line center biases (up to a kHz from direct numerical tests) if the number of fitted data points to the right and to the left of the line center is not the same. We thus implemented a two-pass fit procedure allowing automatic trimming of the fitting window (after the first pass) to make it symmetric around the Lamb dip center.

Let us consider Lamb dip profiles resulting from analyzing the recorded ring-downs with increasing values of PS, corresponding to decreasing laser power I_{PS}. As shown on the top of figure 4, we generally find that the Lamb dip profile grows stronger and narrower up to a maximum intensity, then starts loosing contrast while keeping narrowing over an increasing noise level. In the high power limit, we should be observing the effect of power broadening due to molecules with velocity closer to zero reaching a strong saturation regime. In this regime, the population displaced to the upper transition level approaches 50% and cannot keep increasing as fast as a function of optical power. In the low power limit, on the other hand, the occurring linewidth narrowing may be associated to another known effect, where only slow molecules in the tail of the Maxwell distribution remain sat-

urated and contribute to the Lamb dip, since they experience a larger interaction time with the light beam.[37]

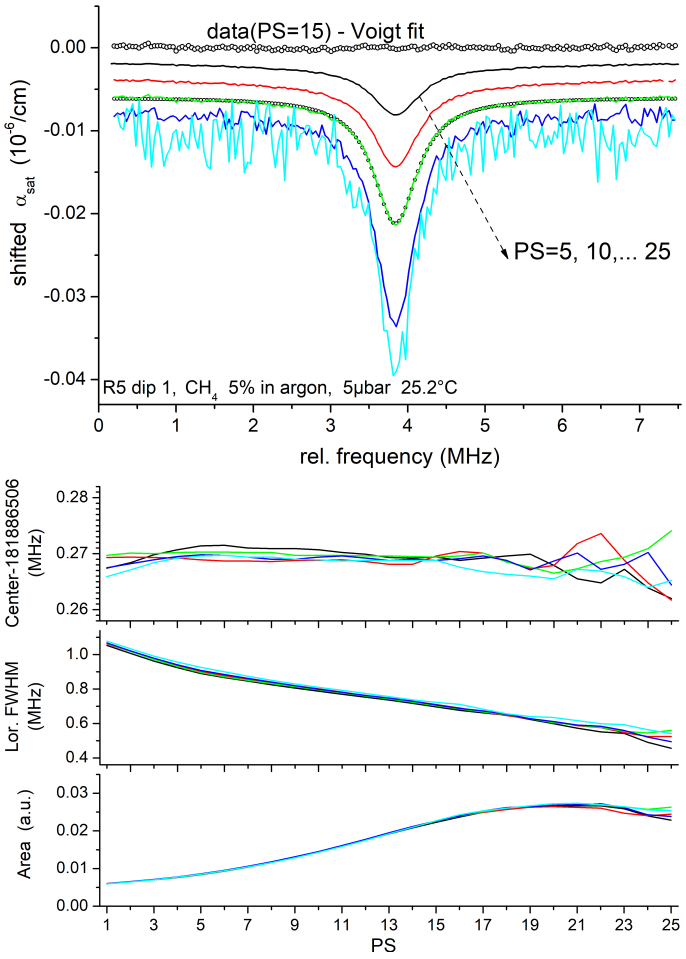

Fig. 4 Top: Typical dependence of Lamb dip profile on power (here for one of the R5 Lamb dips), obtained by skipping PS data points at the beginning of the ring-down decay (spectra are vertically shifted for clarity). Also shown (empty circles) is the Voigt fit (resulting almost Lorentzian) and its residuals for the PS=15 profile (optimal power saturation level). Bottom: dip profile parameters as a function of PS for several scans. The dispersion of center values is minimal around PS=15, where the dip profile signal/noise is close to maximum and the dip width significantly reduced.

As a result of this general behavior of the dips line profile, center frequencies determined from successive spectral scans present a minimum variance for values of PS maximizing the dip intensity, for which the signal/noise on the profile is close to maximal and the linewidth is already significantly reduced. This can be seen on the bottom of figure 4, where Lamb dip line parameters are plotted against PS and for several spectral scans. It should be noticed that a shift of the line center is sometimes observed (as for the dip in the figure) at high saturation levels (small PS). As seen here however, not all collected scans show the same trend, which is therefore not systematic. We are not certain of the source of this effect even though it seems associated to an asymmetric distortion of the line profile, which disappears at moderate power levels where the higher signal/noise of the line profiles should actually make a distortion more visible in the fit residuals. At the same time, in this optimal PS region, the line center is seen to become independent, over several scans, from PS. This situation is found for all the measured dips and guarantees a non critical choice, for the determination of the transition frequency, of an optimal PS to be used for fitting the ring-down decays in all the recorded scans for each dip.

Transition frequencies: Error analysis

Table 1 collects all results of Lamb dips profile fits, except for the Gaussian width which is basically zero within fit statistical error. Since several spectral scans were obtained for each dip, leading to several independent measurements of its position (from 5 up to 356 determinations), a standard error of the mean dip position is obtained directly. This statistical error, reported in the table, may approach 100 Hz in case of a large number of measurements or of particularly high signal/noise in the recorded spectra (e.g. those obtained with non diluted methane).

In addition to statistical errors, several factors in the previously described data processing protocol are prone to introduce systematic biases in the estimation of the dips positions. For each factor we made a reasonable choice for its variability, then we numerically estimated the corresponding variation in the position of each dip. We then composed the resulting errors as for independent random variables in order to determine a global systematic error, which is then composed with the statistical error to give the value in the column “Error” of table 1.

The considered data processing factors and their variations are as follows. As a first factor we consider the ring-down model itself, and for its variation we take the worst–case model, which is the pure exponential decay. A second factor, closely related to the previous, is the saturation level expressed by the PS parameter, for which we consider variations by incrementing or decrementing the initially chosen optimal value by 1. Third is the dip profile fitting model, where we consider that changing the fit baseline polynomial order is already an important model change, thus from a straight line (our default choice for fitting all dips) to a parabola. Moreover, we also considered changing the width and centering of the high resolution spectral fitting window by 10% and by 1 point, respectively. Again, we insist that these variations correspond to estimations of possible maximum variations in the choice of these parameters which may have occurred when setting up the fit of each Lamb dip spectral profile.

Interestingly, the global systematic errors are found to be often comparable to the statistical errors. This is quite satisfactory as it indicates that the experimental effort put into highly accurate measurements was not excessive. More importantly, even changing to a simple exponential fit of the saturated ring-downs still yields dip positions displaced by at most a few times the statistical error. This shows that our choice of a better ring-down fitting model, even though still approximate, is sufficient in reducing model biases below the present data noise level.

Finally, we have to consider physical sources of bias in the dips positions: The transverse relativistic (or second order) Doppler shift and the pressure shift. Other usually considered effects, associated to the recoil and the curvature of field wave fronts, are

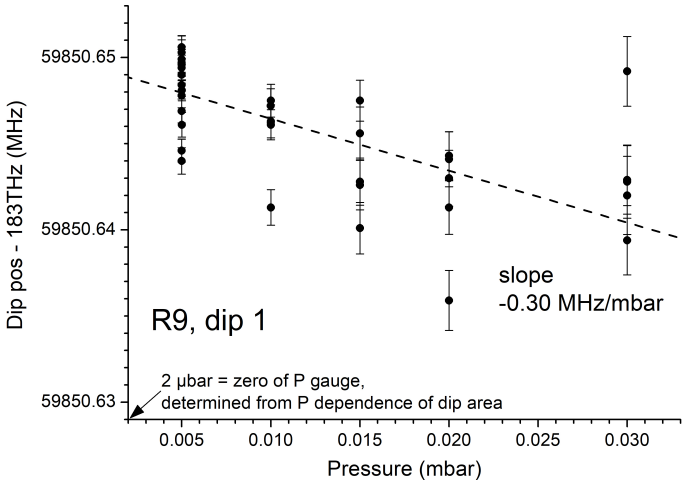

Fig. 5 Pressure dependence of the position of one of the R9 Lamb dips. The slope of a weighted linear fit provides the pressure shift coefficient, whose value falls in agreement with linear regime pressure shifts from the HITRAN database.

negligible or not relevant here. Concerning the recoil, this induces a doublet structure in the Lamb dip which is not resolved here, as in most Lamb dip measurements. The two doublet components are associated to absorption and to stimulated emission by molecules in the lower and upper levels of the transition, respectively.[38] They have same intensity and equal and opposite recoil shifts relative to the transition frequency, so their overlap results in a small broadening with no shift of the observed dip. Concerning the cavity modes wave fronts, in our case their curvature radius is large since the cavity is close to confocal (with mirrors of 1 m radius). Moreover, the excitation and probe fields are counter-propagating progressive waves of same intensity (forming the stationary field of the excited cavity mode), which was shown to be a condition for negligible wave front curvature shift of a Lamb dip.[39]

The relativistic (second order) Doppler shift is associated to the apparent slowing down of a clock moving with constant speed relative to an observer. Thus, a molecule with transverse speed β in the sample (in units of c, the speed of light), absorbing or emitting a photon of frequency ν_0 in its own referential, will actually absorb or emit a photon shifted by $-\beta^2\nu_0/2$ (in the limit $\beta \ll 1$). In our case, averaging over the transverse speed of molecules (the longitudinal component being close to zero for Lamb dip molecules) gives a shift of $-\nu_0\beta_{rms}^2 = -\nu_0 kT/mc^2 \simeq -308\,\mathrm{Hz}$.

Concerning the pressure shift, several scans were obtained of three of the R9 dips, for each of a few pressure values from 5 to 30 μbar of 5% methane diluted in argon. Figure 5 shows the results for one of the dips, where the effect is clearly detectable even at these low pressures. From the slope of the dip positions *versus* pressure the shift coefficient is estimated to a value -0.30 MHz/mbar with standard error 0.06 MHz/mbar. Slopes for the other two dips fall very close (-0.32 and -0.31 MHz/mbar). The average value of -0.31±0.02 MHz/mbar is in good agreement with an average air pressure shift value -0.36 MHz/mbar from linear spectroscopy in the Doppler regime on this methane ro-vibrational band.[40] Regarding the possible difference in values due to air or argon host gases, we can argue that the collisional effects should be rather close due to similar polarizability of air and argon molecules.

Concerning the dependence of dips linewidths on pressure, which we could also deduce from the above measurements, we find a pressure broadening coefficient in argon of 12.6±0.3 MHz/mbar, which is about 7 times larger than the values of broadening coefficient in air listed in the HITRAN database for these absorption lines. This increase of the pressure broadening slope at very low pressure may be attributed to the contribution of elastic velocity changing collisions, which becomes much smaller at higher pressure and for Doppler limited line profiles.[41] It is interesting to compare to results recently published by Twagirayezu *et al.*[42] for saturation dips obtained in a combination band of acetylene in the near infrared, for the same pressure range as here. Their findings are very similar to ours, down to the actual values of shift and broadening coefficients. First of all, they measure a shift coefficient just slightly smaller than literature values for the higher-pressure Doppler regime. Secondly, they find pressure broadening coefficients 4 times larger than at higher pressures. Twagirayezu *et al.* also give a brief review of reports on Lamb dip pressure shifts (very few exist) and they find similar situations. They conclude that "...there is little or no pressure-induced shift seen in most of the sub-Doppler experiments and theoretical consideration of this phenomenon in the literature is sparse or non-existent."

Even though this point should be verified experimentally on a larger sample of dips, we assume here that we should be improving our transition values by applying to all a correction based on the above determined pressure shift coefficient. The resulting correction of the dips positions is +1.5 kHz for 5 μbar, clearly not negligible relative to previously discussed statistical and systematic error bars.

With respect to the R0 to R3 multiplets which we measured at lower pressure (2.75 μbar) but with pure methane, we then consider the linear regime self-shift coefficient found in the literature,[43] whose average value is around -0.51 MHz/mbar, and calculate an almost identical overall correction of +1.4 kHz. As the fractional error or line to line variability associated with these corrections appears to be around 10% (150 Hz), this introduced statistical error is negligible relative to other errors considered before.

Table 1 then lists the dip positions, both in units of wavenumbers and Hertz, corrected for the pressure shift and the second order Doppler shift, together with the corresponding statistical errors and the total errors resulting after combining statistical and systematic errors, by considering them as independent (square root of the sum of squared errors). We should note that in a few cases we detected (unfortunately, after the end of the measurement campaign) that some measurement sets are affected by bad locking of the comb to the optical reference. For the corresponding values we cannot therefore be confident that they are not affected by a larger systematic error than estimated by the above procedure. Therefore, we do not provide the total error for these measurements.

Table 1 Dips frequencies (corrected for the pressure shift and the relativistic Doppler shift) and other relevant parameters for the R0-R10 transitions in the $2\nu_3$ band of $^{12}CH_4$. R0-R3 dips were recorded with pure CH_4 at 2.75 μbar, others with 5% CH_4 in argon at 5.0 μbar. Error values include statistical and systematic errors ($E = \sqrt{E_{stat}^2 + E_{syst}^2}$), as discussed in the text. Notes: (*) frequencies may be affected by larger experimental errors or biases due to problems with the comb frequency locking (systematic error cannot be estimated). (**) comb was self referenced rather than locked to the optical reference (noisier measuremens but still absolute accuracy).

Transition	Wavenumber (cm^{-1})	Frequency (MHz)	Error (kHz)	# scans	Stat. Err. (kHz)	Area (a.u.)	FWHM (MHz)
R0	6015.663827264	180345064.5277	0.23	15	0.11	0.2010	0.700
R1	6026.226861221	180661736.3191	0.44	5	0.32	0.2080	0.707
R2-1	6036.653878668	180974330.4381	0.33	220	0.15	0.2243	0.727
R2-2	6036.657604517	180974442.1363	0.32	220	0.10	0.3310	0.745
R3-1 *	6046.942069191	181282762.6306	-	5	0.56	0.3359	0.756
R3-2 *	6046.951708011	181283051.5952	-	5	0.29	0.4124	0.725
R3-3 *	6046.963578692	181283407.4692	-	5	0.29	0.6230	0.763
R4-1	6057.079461325	181586674.0012	0.57	5	0.48	0.0310	0.734
R4-2	6057.091767924	181587042.9437	0.43	5	0.15	0.0200	0.713
R4-3	6057.100479274	181587304.1035	1.32	5	1.18	0.0126	0.706
R4-4	6057.126601403	181588087.2252	0.90	5	0.75	0.0182	0.739
R5-1	6067.080789296	181886506.2707	0.73	5	0.21	0.0173	0.717
R5-2	6067.098867093	181887048.2295	0.73	5	0.20	0.0172	0.712
R5-3	6067.147313718	181888500.6227	0.53	5	0.19	0.0099	0.728
R5-4	6067.155883254	181888757.5310	0.87	5	0.51	0.0170	0.698
R6-1	6076.927593566	182181706.0363	0.89	6	0.55	0.0091	0.700
R6-2	6076.934108524	182181901.3498	0.83	6	0.57	0.0140	0.716
R6-3	6076.953099148	182182470.6744	0.76	6	0.31	0.0225	0.744
R6-4	6077.027987942	182184715.7840	0.65	10	0.42	0.0134	0.734
R6-5	6077.046452636	182185269.3416	0.54	10	0.36	0.0136	0.728
R6-6	6077.062939662	182185763.6102	0.66	10	0.28	0.0215	0.739
R7-1	6086.622405184	182472349.1768	0.61	10	0.35	0.0110	0.739
R7-2	6086.634248348	182472704.2259	0.77	10	0.32	0.0108	0.734
R7-3 **	6086.744561511	182476011.3313	0.61	356	0.09	0.0184	0.756
R7-4 **	6086.778835432	182477038.8377	0.51	356	0.11	0.0100	0.744
R7-5 **	6086.798099382	182477616.3563	0.81	356	0.14	0.0077	0.748
R7-6 **	6086.829780492	182478566.1321	0.81	356	0.11	0.0110	0.756
R8-1	6096.167038655	182758490.0897	0.88	54	0.36	0.0144	0.661
R8-2	6096.175408943	182758741.0246	1.15	54	0.56	0.0088	0.639
R8-3	6096.180097555	182758881.5857	1.86	54	0.95	0.0062	0.633
R8-4 *	6096.371781084	182764628.1133	-	38	0.34	0.0081	0.688
R8-5 *	6096.423376813	182766174.9143	-	6	0.92	0.0085	0.689
R8-6 *	6096.484555863	182768009.0161	-	6	2.77	0.0058	0.673
R8-7 *	6096.500332351	182768481.9833	-	6	0.53	0.0084	0.664
R9-1	6105.624327136	183042012.4657	1.10	6	0.64	0.0055	0.728
R9-2	6105.625798126	183042056.5648	1.58	6	0.89	0.0054	0.714
R9-3	6106.036582138	183054371.5597	2.19	6	2.08	0.0033	0.706
R9-4	6106.042877610	183054560.2932	2.10	6	1.84	0.0051	0.683
R9-5	6106.050522295	183054789.4751	1.33	6	0.58	0.0087	0.733
R9-6	6106.219344915	183059850.6499	1.15	6	0.56	0.0027	0.605
R9-7	6106.250676203	183060789.9383	1.37	6	0.93	0.0028	0.613
R9-8	6106.282909981	183061756.2827	0.92	6	0.46	0.0052	0.625
R10-1	6114.479280096	183307477.2770	2.31	6	2.03	0.0024	0.694
R10-2	6114.484043371	183307620.0764	2.23	6	1.99	0.0033	0.685
R10-3	6114.495790334	183307972.2415	1.57	6	1.02	0.0056	0.711
R10-4	6114.549500834	183309582.4418	4.02	6	3.55	0.0021	0.645
R10-5	6114.561196215	183309933.0605	4.21	6	2.48	0.0010	0.570
R10-6	6114.610565314	183311413.1088	2.49	6	2.06	0.0022	0.673
R10-7	6114.661127452	183312928.9236	0.92	6	0.70	0.0061	0.692
R10-8	6114.670689513	183313215.5870	3.72	6	3.00	0.0014	0.572
R10-9	6114.672321116	183313264.5012	2.24	6	1.82	0.0028	0.638
R10-10	6114.676537015	183313390.8907	3.31	6	2.78	0.0023	0.607
R10-11	6114.677675243	183313425.0139	1.88	6	1.53	0.0031	0.654

As a qualitative information, the table also lists Lamb dips areas (in arbitrary units) and Lorentzian widths (FWHM). As discussed earlier, these depend on the saturation level embodied by the optimal PS parameter chosen to maximize signal/noise. The PS values are however not listed since they would hardly be useful since the corresponding real power levels depend on a few other experimental conditions, such as the photodetector gain or the cavity mirrors losses, which were subject to changes during several days of measurements.

With respect to the widths, one can see that their values are rather uniform and all comprised between 600 and 750 MHz. Finally, regarding the Lamb dip areas, their value is obviously very large for the few low-J measurements obtained in pure methane, where also the total line absorption is high, which is evident by looking at the vertical scales in figure 2. On the other hand, dips areas are seen to decrease uniformly for all other higher-J measurements obtained with 5% methane in argon, which just corresponds to the line intensities of multiplets decreasing steadily with rotational excitation. Correspondingly, we also see that the error bars on the transition frequencies increase.

4 $^{12}CH_4$ transition frequencies in the $2\nu_3$ band

Literature review

The strong $2\nu_3$ band of methane centered near 6005 cm^{-1} features a strong and highly congested Q branch and a mostly regular P and R branches separated by about 10 cm^{-1} and composed of well isolated multiplets. Due to its strength and to its spectral location in the important 1.58 μm atmospheric transparency window, this band has a particular importance for atmospheric retrievals of methane from the ground or from satellites. The Total Carbon Column Observing Network (TCCON) uses the $2\nu_3$ band to retrieve the methane concentration from long path atmospheric spectra recorded by Fourier Transform Spectroscopy (FTS).[44] SCIAMACHY on board of ENVISAT satellite uses a microwindow corresponding to strong Q and R multiplets to monitor methane with very high sensitivity for the entire atmospheric column.[45–47] The Greenhouse gases Observing SATellite (GOSAT) launched in 2009 uses the same $2\nu_3$ band to measure CH_4 concentration in the near surface layers.[48] The future MEthane Remote sensing LIdar mission (MERLIN) of the French (CNES) and German (DLR) space agencies, will obtain spatial and temporal gradients of atmospheric methane (CH_4) columns, on a global scale, using the R6 multiplet of the $2\nu_3$ band.[49,50]

Systematic biases in the methane concentration retrieval may be introduced by an insufficient knowledge of the CH_4 spectroscopy of the $2\nu_3$ band. The detailed line profile modeling of the $2\nu_3$ multiplets in atmospheric conditions is crucial to achieve the high precision and unprecedented accuracy targeted by satellite missions such as MERLIN. The modeling is made difficult by the number of overlapping lines (or components) strongly broadened and shifted by pressure effects, contributing to the multiplets. Even at low pressure, in the Doppler regime, a significant part of the components cannot be resolved. For instance, recent laboratory work has been dedicated to the improvement of the description of the air-broadened absorption of the R6 multiplet.[50,53]

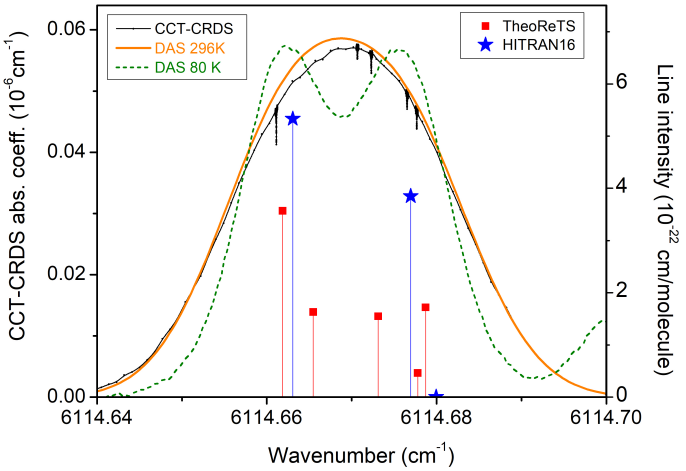

Fig. 6 Comparison of the spectrum of a part of the R10 multiplet recorded by direct absorption spectroscopy at room temperature and at 80 K[51] (orange and dotted green, respectively) to a spectrum presently recorded by CCT-CRDS (black solid line). Five dips are observed in the saturation regime while this multiplet is represented by a doublet in the HITRAN2016 list (blue sticks). According to the TheoReTS calculated list (red sticks)[52] five transitions are indeed predicted to contribute to the observed absorption feature.

Six components contribute to the mostly unresolved R6 absorption feature observed in atmospheric conditions. A total of more than forty line parameters were retrieved from a fit of a series of room temperature spectra at various pressures, recorded by frequency-stabilized CRDS. In order to decorrelate some of the needed parameters from the others (in particular the pressure shifts), constraints on the zero-pressure positions provided by independent measurements would be highly valuable.

At present, line positions and line intensities relative to the $2\nu_3$ band provided by the HITRAN[33] and GEISA[54] spectroscopic databases are empirical values retrieved from low pressure spectra of pure methane. The current version of the HITRAN database uses as main source of $2\nu_3$ line parameters a study performed in support of the GOSAT mission based on a series of recordings by Fourier Transform Spectroscopy (FTS),[55,56] mostly at room temperature. The uncertainty attached to the $2\nu_3$ GOSAT position values in HITRAN2016 is a conservative value of 0.01 cm^{-1} (or 300 MHz).

As discussed in the introduction, in addition to the uncertainty due to the line centre determination of blended lines, the frequency calibration of the recorded spectra contributes to the error budget of the reported line centres. Spectra of the $2\nu_3$ region directly referenced to atomic frequency standards have been recorded by dual comb spectroscopy.[57] In order to avoid uncertainties related to line overlapping, Zolot *et al.* limited their measurements to well isolated lines. Line centers with sub-MHz accuracy ($< 3\times10^{-5}$ cm^{-1}) were reported for about forty strong lines of the $2\nu_3$ band, including a ten of R branch lines in common with our measurements which will be discussed below. Part of the dual-comb line positions were preferred to GOSAT line positions and incorporated into the HITRAN2016 list with error bars of 10^{-3} or 10^{-4} cm^{-1}.

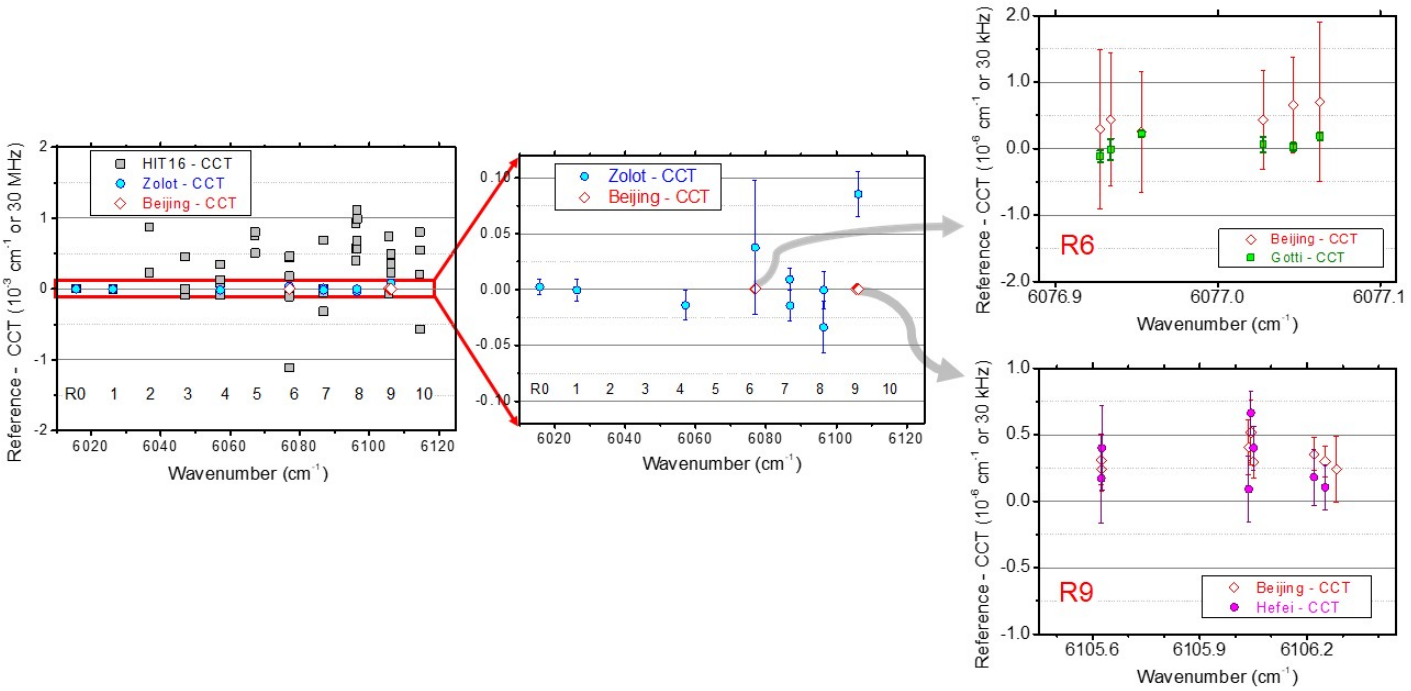

Fig. 7 Line centers comparison of the R0-R10 multiplets of the $2\nu_3$ band of $^{12}CH_4$. Left panel: Deviations from the CCT dip values of the centers provided by the HITRAN2016 database (squares), measured in the Doppler regime in [57] (circles) and in the saturation regime by the Beijing group [20,58] (diamonds). Middle panel: Zoom limited to Zolot measurements (with corresponding error bars) and to the dip centers of the Beijing group. Right panels: Focus of the R6 and R9 multiplets studied in the saturation regime. The R6 comparison applies to the results of Beijing [20] and Gotti [17] (diamonds and squares, respectively). The R9 comparison considers the results of Beijing [59] and Hefei [58] (diamonds and circles, respectively).

In the case of methane, the precision on the line centre determination of blended lines in the Doppler regime, can be significantly improved by low temperature recordings. Indeed, methane can be cooled down to liquid nitrogen temperature (77 K) which reduces the Doppler width by about a factor of 2 and helps to resolve multiplets.[60] The region of the $2\nu_3$ band of methane was recorded at 80 K by differential absorption spectroscopy (DAS).[51,61–63] The comparison of a R10 multiplet at 296 and 80 K presented in figure 6 shows that a doublet structure is partly resolved at 80 K while it appears as a single line at 296 K (note that, in fact, five R10 components contribute to the observed absorption feature).

The DAS spectra of Campargue *et al.*[51,63] provided a significant gain in term of sensitivity compared to GOSAT FTS spectra.[55] The results of the DAS analysis in the $2\nu_3$ region were incorporated into the WKLMC (Wang, Kassi, Leshchishina, Mondelain, Campargue) methane empirical covering the 5855-7912 cm^{-1} range,[64] particularly suitable for planetary applications.[65,66]

To the best of our knowledge, the first measurements of sub-Doppler saturated absorption (Lamb dips) in the $2\nu_3$ band of methane were reported in the 90s in the group of Sasada of the Keio University in Yokohama (Japan).[68–70] Optical frequency combs were not available at that time and precise frequency differences between $2\nu_3$ transitions were obtained as the optical beat frequency between two external-cavity diode lasers locked at 1-MHz-wide saturated absorption dips of the methane lines. A number of frequency differences mostly between Q-branch transitions of the of the $2\nu_3$ band were reported with a precision better than 40 kHz. Finally, in 1999, the Yokohama group implemented an optical frequency comb and the absolute frequency of the $2\nu_3$ R0 and Q1 transitions could be determined with an accuracy of 600 kHz.[16]

These last years, Lamb dip CRDS was applied to the R6 and R9 multiplets of the $2\nu_3$ band. First, in Gotti *et al.*[17], the R6 multiplet was explored as a first illustration of the CCT-CRDS method and Lamb dip positions of the six R6 components were reported with statistical uncertainty in the kHz range. Yang *et al.*[22] applied temperature-scanning saturation CRDS to the measurement of the position of one of the R6 components which they reported with an uncertainty of 20 kHz. Comb-linked frequency-stabilized CRDS was used by the same group (Beijing group, hereafter) to determine the position of the R9 components with an average accuracy of 5 kHz.[59] Very recently, the Beijing group performed new Lamb dip measurements in the R6 region and reported the center of 18 Lamb dips (including the six R6 components) with an accuracy between 15 and 60 kHz (5×10^{-7} and 2×10^{-6} cm^{-1}).[20]

Finally, in Liu *et al.*[58], a detailed study of the R9 region was performed in Hefei (China) by saturated CRDS: 32 dip centers were determined in the 6105.3–6107.3 cm^{-1} spectral interval, with an accuracy of a few kHz, extending significantly the eleven dip Beijing measurements in the region.[59] The Hefei measurements include (i) the eight R9 strong components, (ii) weaker lines belonging to other vibrational bands and listed in the HITRAN database (iii) three new weak transitions obscured by the R6 multiplet in the Doppler regime. In particular, the Hefei dip measurements questioned the discovery of some weak CH_4 lines

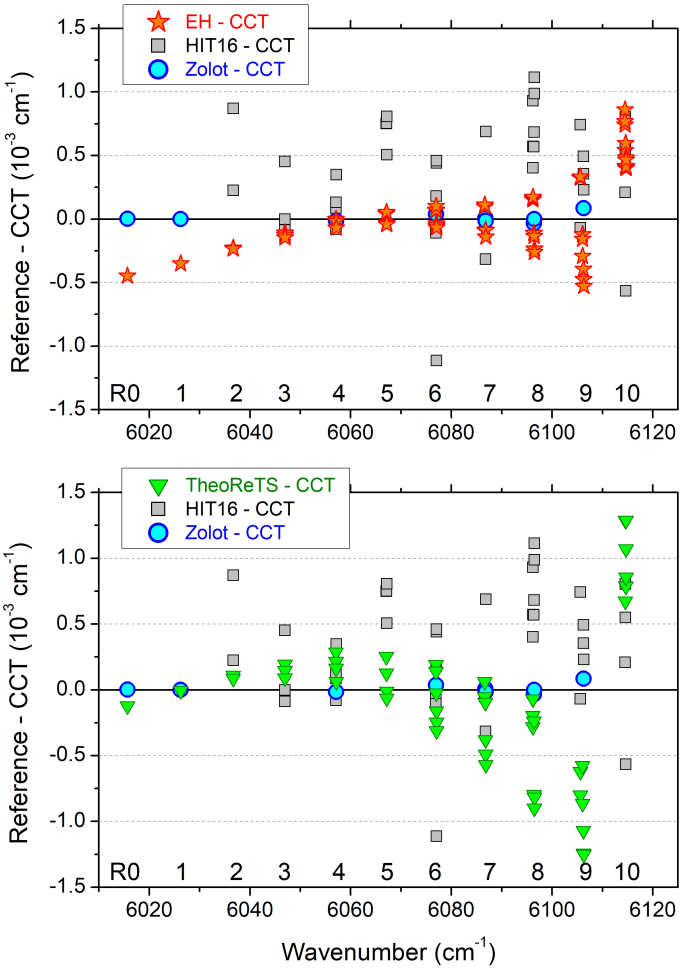

Fig. 8 Deviations of measured line centers of R0-R10 multiplets of the $2\nu_3$ band of $^{12}CH_4$ from transition frequencies calculated by an effective Hamiltonian[67] (upper panel, stars) and from the TheoReTS values[52] (lower panel, triangles). For completeness, deviations from HITRAN2016 values and Zolot measurements[57] are plotted (squares and circles, respectively).

reported by the Beijing group from Doppler spectra.[59]

Comparison to previous measurements

Figure 7 compares our zero-pressure CCT dip centers to HITRAN line positions and to the 9 centers of well isolated lines reported in the Doppler regime by Zolot *et al.*[57]. For HITRAN multiplets, the comparison applies only in the case of clear one-to-one correspondence with dip measurements and excludes blended lines situations such as that presented in figure 6. An agreement with Zolot values within their claimed uncertainty, on the order of 10^{-5} cm^{-1}, is observed for the lines in common. The only exception is the R9 line at 6106.25117 cm^{-1} which deviates from our CCT value by nearly 10^{-4} cm^{-1}, more than 4 times the error bar given by Zolot. Note that our position value agrees with Beijing[59] and Hefei[58] measurements within a few 10^{-7} cm^{-1}. As mentioned above, HITRAN2016 reproduces some of the positions reported by Zolot with error bars of 10^{-3} or 10^{-4} cm^{-1}, thus significantly larger than the original uncertainty values. The other HITRAN values use the GOSAT-2014 list[56] as source and are also provided with a conservative error bar (10^{-2} cm^{-1}), largely exceeding the average agreement with our values, on the order of 10^{-3} cm^{-1}.

As concerns the comparison to previous dip measurements in the R6 and R9 multiplets, an average agreement on the order of 5×10^{-7} cm^{-1} (15 kHz) is achieved between the present CCT and Beijing R6 measurements[20] (right upper panel in figure 7). This is well within the typical 30 kHz accuracy of Beijing values. An even better agreement is noted with the R6 CCT dip centers reported by Gotti *et al.*[17] with average differences on the order of 10^{-7} cm^{-1} (3 Hz). These last values were obtained with a first version of our CCT setup, and no serious effort was used to produce an accurate error budget since the aim was mainly about demonstrating the performance of a CCT source.

The dip centers of the eight components of the R9 multiplet can be compared to Beijing[59] and Hefei[58] dip centers reported with similar accuracies on the order of 2-3$\times10^{-7}$ cm^{-1} (6-9 kHz). On average, there is a coincidence at the kHz level between the Beijing and Hefei values while the present CCT values, reported with 1-2 kHz accuracy, appear to be on average smaller by about 10 kHz (right lower panel in figure 7). This small disagreement being barely outside the combined measurements error bars, it should not be considered as meaningful.

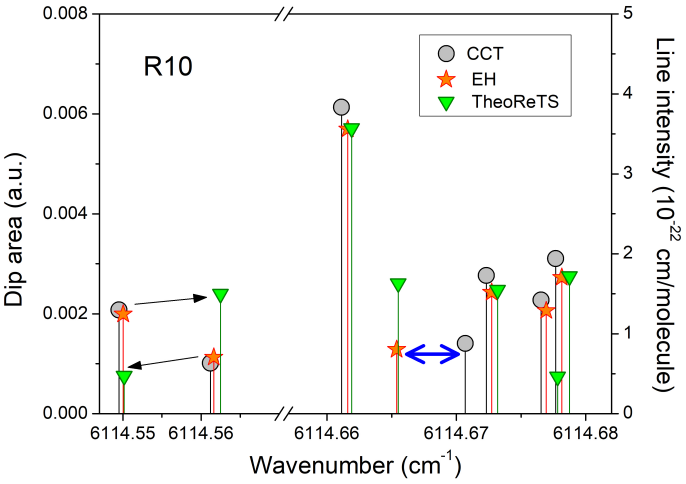

Fig. 9 Superposition of the stick spectrum calculated using the effective operator approach[67] (stars) to the TheoReTS line list[52] (triangles) and to our CCT measured dips (circles) in the region of the high frequency component of the R10 multiplet. The ordinate scale of the dip spectrum corresponding to the dip area has been scaled to match the intensity scale of the calculated line list. The blue arrow points the transition corresponding to the largest (EH-CCT) position difference. The black arrows highlight the two components of the doublet near 6114.55 cm^{-1} which have TheoReTS intensities inverted compared to both the EH and dip spectra.

Comparison to calculated line lists

Here, we compare our experimental values to the $2\nu_3$ transition frequencies provided by theory. Contrary to experimental lists derived from spectra in the Doppler regime where some highly blended components cannot be resolved, calculated line lists have the advantage to include all the components of the different

multiplets. In principle, this makes it possible an unambiguous one-to-one correspondence between dip measurements and calculated line centers.

Let us first consider the line centers computed using the effective Hamiltonian (EH) approach[71,72]. Due to the high tetrahedral symmetry, some vibrational normal modes are doubly or triply degenerate in the CH_4 molecule. These degeneracies combined with accidental resonances between the harmonic frequencies $\omega_1 \simeq \omega_3 \simeq 2\omega_2 \simeq 2\omega_4$ lead to an organization of the vibrational levels in clusters or polyads. Each polyad gathers nearby vibrational levels corresponding to the same value of the polyad number $P = 2V_1 + V_2 + 2V_3 + V_4$ ($V_{i=1-4}$ are the corresponding quantum numbers). The upper level of the $2\nu_3$ band under study belongs thus to the $P = 4$ polyad namely, the tetradecad. The most recent modeling of the $^{12}CH_4$ spectrum in the tetradecad was reported in Nikitin *et al.*[67]. Considering the number of tetradecad levels (14 levels and 60 sublevels), the number of adjustable EH parameters in the tetradecad is considerable and a combined approach is applied[71,72] using as initial EH, an EH polyad model derived from an *ab initio* molecular potential energy surface (PES)[73] *via* a high order contact transformation. This method provides realistic estimates for the rovibrational coupling parameters and reduces the number of parameters fitted on measured line positions. It was applied successfully to extend the assignments in the high energy part of the tetradecad including the $2\nu_3$ band (5855-6250 cm^{-1}) where a total of more than 3200 $^{12}CH_4$ line centres could be reproduced with an *rms* measured-minus-calculated deviation of 1.5×10^{-3} cm^{-1} .[71] Figure 8 shows the position comparison between the most recent EH calculations and our CCT dips measurements in the $2\nu_3$ R branch. The overall agreement is very good, significantly better than compared to the HITRAN2016 database. Except for $J = 10$, all deviations are within $\pm5\times10^{-4}$ cm^{-1} and show smooth J dependence. The tendency is broken for the $J = 10$ multiplet which deviates by 5-8$\times10^{-4}$ cm^{-1} which is larger by about 10^{-3} cm^{-1} compared to the expected general tendency. In fact, a much larger outlier is not plotted on figure 8. It concerns the R10 dip at 6114.670689 cm^{-1}. The comparison of the stick spectra displayed presented in Fig.9 indicates that this dip must be associated to the EH transition with wavenumber smaller by 5.3×10^{-3} cm^{-1} (blue arrow in figure 9). Note that this correspondence is supported not only by the fact that a one-to-one correspondence is found for all the other R10 dips but also by the good agreement between the dip area and the EH line intensity.

We have also included in figure 8 (lower panel) a comparison of the dip centers to the TheoReTS calculated line list accessible *via* the TheoReTS information system (http://theorets.univ-reims.fr, http://theorets.tsu.ru). This list was computed by variational method[52] using the ab initio ACV5Z dipole moment surface.[74] In terms of transition frequencies, theoretical methods do not reach experimental accuracy. As far as possible, in the TheoReTS list, variational positions were replaced either by positions calculated from empirical values of the upper and lower energy levels or by positions provided by EH calculations. A tag is attached to the corrected TheoReTS positions but empirical or EH corrections cannot be discriminated. The (TheoReTS-CCT) deviations presented on the lower panel of Fig.8 show a similar dependence as the (EH-CCT) deviations indicating that the TheoReTS positions were adjusted according to EH calculations. Nevertheless, overall the deviations are larger probably due to the use of a previous version of the EH. In particular, deviations are more pronounced (and of opposite sign), for $J = 9$ and 10. This could be the signature of a local resonance interaction with an energy crossing between $J = 9$ and 10, which is better accounted for by the most recent version of the EH. Although reduced, the remaining effect might explain the gap between the (EH-CCT) deviations of $J = 9$ and 10. Finally, the TheoReTS stick spectrum included in figure 9 shows some disagreements for the line intensities of the R10 multiplet. For instance, the line intensities of the two components of the doublet near 6114.55 cm^{-1} appear to be inverted compared to both the EH predictions and the dip measurements. These differences might concern transitions which have EH positions and/or line intensities strongly affected by small changes of the EH parameters and thus very sensitive to the suspected resonance interaction.

5 Conclusions

In order to obtain highly accurate transition frequencies for rovibrational transitions in methane, we applied a newly developed CCT laser source directly derived from an optical frequency comb (itself locked to a SI-traceable optical frequency reference). Besides being frequency accurate and spectrally narrow, this source is broadly tunable with local agility, robust and easy to operate leading to efficient acquisition of large amount of spectral data. In combination with cavity ring-down spectroscopy, the CCT spectral purity allows large intracavity power buildup readily saturating weak vibrational overtone transitions. in particular, the counter propagating intracavity optical fields allow the formation of sub-Doppler Lamb dips from zero velocity class molecules, a spectral feature giving the most precise evaluation of the molecular transition frequencies.

The CCT-CRDS setup was applied to determine with unprecedented accuracy the line centers of the R0-R10 multiplets of the $2\nu_3$ band of $^{12}CH_4$. This band is of particular interest for the methane monitoring in our atmosphere both from ground based spectrometers (e.g. the FTS spectrometers of the Total Carbon Column Observing Network) and from space (e.g. SCIAMACHY, GOSAT and the future MERLIN mission). Under atmospheric conditions, the structure of the $2\nu_3$ multiplets is mostly unresolved due to line pressure broadening. Accurate retrieval of methane concentration is thus made particularly challenging. The sophisticated line profiles required to achieve the targeted accuracy involve a large number of parameters, including their temperature dependence and line mixing effects, which have to be determined from a fit of the recorded absorption spectra[50,53].

Tight constraint on the line positions obtained from laboratory spectra as in the present work, will provide a valuable help to decorrelate part of the line profile parameters from the others. In addition, the set of more than 50 line centers obtained with an accuracy for half of them better than 1 kHz and for the rest below 4 kHz ($< 1.3\times10^{-7}$ cm^{-1}) will be valuable for improving spectroscopic databases such as HITRAN and to provide stringent

validation tests for the most advanced theoretical modeling of the methane absorption spectrum.

Conflicts of interest

There are no conflicts to declare.

Acknowledgments

O.V. is grateful to CNRS for the visiting program allowing his stay in Grenoble. We acknowledge funding support from the Agence Nationale de la Recherche (Equipex REFIMEVE+ ANR-11-EQPX-0039 and e_PYTHEAS ANR-16-CE31-0005). In the frame of the REFIMEVE+ project we are particularly grateful to P.E. Pottie, E. Cantin, and R. Le Targat (LNE-SYRTE, Observatoire de Paris, France) and to A. Amy-Klein (Laboratoire de Physique des Lasers, Villetaneuse, France) for their support and exchanges concerning the remote optical reference frequency. Finally, we thank A. Nikitin (Zuev Institute of Atmospheric Optics Tomsk, Russia) for useful exchanges and for providing the results of the EH calculations in ref[71].

Notes and references

1 L.-S. Ma, Z. Bi, A. Bartels, L. Robertsson, M. Zucco, R. S. Windeler, G. Wilpers, C. Oates, L. Hollberg and S. A. Diddams, *Science*, 2004, **303**, 1843–1845.

2 A. Bartels, C. W. Oates, L. Hollberg and S. A. Diddams, *Optics Letters*, 2004, **29**, 1081–1083.

3 G.-W. Truong, D. A. Long, A. Cygan, D. Lisak, R. D. van Zee and J. T. Hodges, *The Journal of Chemical Physics*, 2013, **138**, 094201.

4 D. A. Long, G. W. Truong, J. T. Hodges and C. E. Miller, *Journal of Quantitative Spectroscopy and Radiative Transfer*, 2013, **130**, 112–115.

5 K. Bielska, S. Wójtewicz, P. Morzyski, P. Ablewski, A. Cygan, M. Bober, J. Domysawska, M. Zawada, R. Ciuryo, P. Masowski and D. Lisak, *Journal of Quantitative Spectroscopy and Radiative Transfer*, 2017, **201**, 156–160.

6 S. Kassi, T. Stoltmann, M. Casado, M. Daëron and A. Campargue, *The Journal of Chemical Physics*, 2018, **148**, 054201.

7 S. Kassi, B. Gao, D. Romanini and A. Campargue, *Physical chemistry chemical physics : PCCP*, 2008, **10**, 4410–4419.

8 S. Kassi, D. Romanini and A. Campargue, *Chemical Physics Letters*, 2009, **477**, 17–21.

9 O. Votava, M. Maát, P. Pracna, D. Mondelain, S. Kassi, A. W. Liu, S. M. Hu and A. Campargue, *Journal of Quantitative Spectroscopy and Radiative Transfer*, 2014, **149**, 64–71.

10 W. Demtröder, in *Laser Spectroscopy*, ed. M. I. Roach, Springer, Berlin, Heidelberg, 2003.

11 W. E. Lamb, *Physical Review*, 1964, **134**, A1429–A1450.

12 T. W. Haensch, I. S. Shahin and A. L. Schawlow, *Nature (London) Phys. Sci. 235: No. 56, 63-5(24 Jan 1972).*, 1972, 63–65.

13 A. L. Schawlow, *Reviews of Modern Physics*, 1982, **54**, 697–707.

14 R. L. Barger and J. L. Hall, *Physical Review Letters*, 1969, **22**, 4–8.

15 M. d. Labachelerie, K. Nakagawa and M. Ohtsu, *Optics Letters*, 1994, **19**, 840–842.

16 C. Ishibashi, M. Kourogi, K. Imai, B. Widiyatmoko, A. Onae and H. Sasada, *Optics Communications*, 1999, **161**, 223–226.

17 R. Gotti, M. Prevedelli, S. Kassi, M. Marangoni and D. Romanini, *The Journal of Chemical Physics*, 2018, **148**, 054202.

18 H. Wu, C.-L. Hu, J. Wang, Y. R. Sun, Y. Tan, A.-W. Liu and S.-M. Hu, *Physical Chemistry Chemical Physics*, 2020, **22**, 2841–2848.

19 T.-p. Hua, Y. Suna, Robert, J. Wang, C.-L. Hu, L.-g. Tao, A.-w. Liu and S.-m. Hu, *Chinese Journal of Chemical Physics*, 2019, **32**, 107–112.

20 L. Yang, H. Lin, M. D. Plimmer, X. J. Feng, Y. J. Ma, J. T. Luo, J. F. Luo and J. T. Zhang, *Journal of Quantitative Spectroscopy and Radiative Transfer*, 2020, **245**, 106888.

21 G. Zhao, T. Hausmaninger, F. M. Schmidt, W. Ma and O. Axner, *Optics Express*, 2019, **27**, 17940–17953.

22 L. Yang, H. Lin, X. J. Feng and J. T. Zhang, *Optics Express*, 2018, **26**, 10203–10210.

23 A. Czajkowski, A. J. Alcock, J. E. Bernard, A. A. Madej, M. Corrigan and S. Chepurov, *Optics Express*, 2009, **17**, 9258–9269.

24 V. D. Sarno, R. Aiello, M. D. Rosa, I. Ricciardi, S. Mosca, G. Notariale, P. D. Natale, L. Santamaria and P. Maddaloni, *Optica*, 2019, **6**, 436–441.

25 J. Burkart, T. Sala, D. Romanini, M. Marangoni, A. Campargue and S. Kassi, *The Journal of Chemical Physics*, 2015, **142**, 191103.

26 F. Cozijn, P. Dupré, E. Salumbides, K. Eikema and W. Ubachs, *Physical Review Letters*, 2018, **120**, 153002.

27 L.-G. Tao, A.-W. Liu, K. Pachucki, J. Komasa, Y. Sun, J. Wang and S.-M. Hu, *Physical Review Letters*, 2018, **120**, 153001.

28 J. Morville, D. Romanini, M. Chenevier and A. Kachanov, *Applied Optics*, 2002, **41**, 6980–6990.

29 T. Sala, S. Kassi, J. Burkart, M. Marangoni and D. Romanini, *Arxiv*, 2014, http://arxiv.org/abs/1412.1102.

30 R. Gotti, T. Sala, M. Prevedelli, S. Kassi, M. Marangoni and D. Romanini, *The Journal of Chemical Physics*, 2018, **149**, 154201.

31 C. Lisdat, G. Grosche, N. Quintin, C. Shi, S. M. F. Raupach, C. Grebing, D. Nicolodi, F. Stefani, A. Al-Masoudi, S. Dörscher, S. Häfner, J.-L. Robyr, N. Chiodo, S. Bilicki, E. Bookjans, A. Koczwara, S. Koke, A. Kuhl, F. Wiotte, F. Meynadier, E. Camisard, M. Abgrall, M. Lours, T. Legero, H. Schnatz, U. Sterr, H. Denker, C. Chardonnet, Y. Le Coq, G. Santarelli, A. Amy-Klein, R. Le Targat, J. Lodewyck, O. Lopez and P.-E. Pottie, *Nature Communications*, 2016, **7**, 12443.

32 E. Cantin, M. Tønnes, R. Le Targat, A. Amy-Klein, O. Lopez and P.-E. Pottie, *New Journal of Physics*, 2021, **23**, 053027.

33 I. E. Gordon, L. S. Rothman, C. Hill, R. V. Kochanov, Y. Tan, P. F. Bernath, M. Birk, V. Boudon, A. Campargue, K. V. Chance, B. J. Drouin, J. M. Flaud, R. R. Gamache, J. T. Hodges, D. Jacquemart, V. I. Perevalov, A. Perrin, K. P. Shine, M. A. H. Smith, J. Tennyson, G. C. Toon, H. Tran, V. G. Tyuterev, A. Barbe, A. G. Császár, V. M. Devi, T. Furtenbacher, J. J. Harrison, J. M. Hartmann, A. Jolly, T. J. Johnson, T. Karman,

I. Kleiner, A. A. Kyuberis, J. Loos, O. M. Lyulin, S. T. Massie, S. N. Mikhailenko, N. Moazzen-Ahmadi, H. S. P. Müller, O. V. Naumenko, A. V. Nikitin, O. L. Polyansky, M. Rey, M. Rotger, S. W. Sharpe, K. Sung, E. Starikova, S. A. Tashkun, J. V. Auwera, G. Wagner, J. Wilzewski, P. Wciso, S. Yu and E. J. Zak, *Journal of Quantitative Spectroscopy and Radiative Transfer*, 2017, **203**, 3–69.

34 D. Romanini, P. Dupre and R. Jost, *Vibrational Spectroscopy.*, 1999, **19**, 93–106.

35 J. Burkart, *Ph.D. thesis*, Grenoble Alpes University, 2002.

36 L. Yang, H. Lin, X. J. Feng, M. D. Plimmer and J. T. Zhang, *Optics Express*, 2019, **27**, 1769–1776.

37 C. J. Bordé, J. L. Hall, C. V. Kunasz and D. G. Hummer, *Physical Review A*, 1976, **14**, 236–263.

38 C. Oates, G. Wilpers and L. Hollberg, *Physical Review A*, 2005, **71**, 023404.

39 J. L. Hall and C. J. Bordé, *Applied Physics Letters*, 1976, **29**, 788–790.

40 O. M. Lyulin, A. V. Nikitin, V. I. Perevalov, I. Morino, T. Yokota, R. Kumazawa and T. Watanabe, *Journal of Quantitative Spectroscopy and Radiative Transfer*, 2009, **110**, 654–668.

41 L. S. Vasilenko, V. P. Kochanov and V. P. Chebotayev, *Optics Communications*, 1977, **20**, 409–411.

42 S. Twagirayezu, G. E. Hall and T. J. Sears, *The Journal of Chemical Physics*, 2018, **149**, 154308.

43 O. M. Lyulin, V. I. Perevalov, I. Morino, T. Yokota, R. Kumazawa and T. Watanabe, *Journal of Quantitative Spectroscopy and Radiative Transfer*, 2011, **112**, 531–539.

44 K. M. Saad, D. Wunch, G. C. Toon, P. Bernath, C. Boone, B. Connor, N. M. Deutscher, D. W. T. Griffith, R. Kivi, J. Notholt, C. Roehl, M. Schneider, V. Sherlock and P. O. Wennberg, *Atmospheric Measurement Techniques*, 2014, **7**, 2907–2918.

45 M. Buchwitz, R. de Beek, S. Noël, J. P. Burrows, H. Bovensmann, O. Schneising, I. Khlystova, M. Bruns, H. Bremer, P. Bergamaschi, S. Körner and M. Heimann, *Atmospheric Chemistry and Physics*, 2006, **6**, 2727–2751.

46 C. Frankenberg, J. F. Meirink, P. Bergamaschi, A. P. H. Goede, M. Heimann, S. Körner, U. Platt, M. v. Weele and T. Wagner, *Journal of Geophysical Research: Atmospheres*, 2006, **111**, D07303.

47 P. Bergamaschi, C. Frankenberg, J. F. Meirink, M. Krol, F. Dentener, T. Wagner, U. Platt, J. O. Kaplan, S. Körner, M. Heimann, E. J. Dlugokencky and A. Goede, *Journal of Geophysical Research: Atmospheres*, 2007, **112**, 1–26.

48 R. Parker, H. Boesch, A. Cogan, A. Fraser, L. Feng, P. I. Palmer, J. Messerschmidt, N. Deutscher, D. W. T. Griffith, J. Notholt, P. O. Wennberg and D. Wunch, *Geophysical Research Letters*, 2011, **38**, L15807.

49 C. Pierangelo, B. Millet, F. Esteve, M. Alpers, G. Ehret, P. Flamant, S. Berthier, F. Gibert, O. Chomette, D. Edouart, C. Deniel, P. Bousquet and F. Chevallier, *EPJ Web of Conferences*, 2016, **119**, 26001.

50 T. Delahaye, S. E. Maxwell, Z. D. Reed, H. Lin, J. T. Hodges, K. Sung, V. M. Devi, T. Warneke, P. Spietz and H. Tran, *Journal of Geophysical Research: Atmospheres*, 2016, **121**, 7360–7370.

51 A. Campargue, O. Leshchishina, D. Mondelain, S. Kassi and A. Coustenis, *Journal of Quantitative Spectroscopy and Radiative Transfer*, 2013, **118**, 49–59.

52 M. Rey, A. V. Nikitin, B. Bézard, P. Rannou, A. Coustenis and V. G. Tyuterev, *Icarus*, 2018, **303**, 114–130.

53 T. Delahaye, M. Ghysels, J. T. Hodges, K. Sung, R. Armante and H. Tran, *Journal of Geophysical Research: Atmospheres*, 2019, **124**, 3556–3564.

54 N. Jacquinet-Husson, R. Armante, N. A. Scott, A. Chédin, L. Crépeau, C. Boutammine, A. Bouhdaoui, C. Crevoisier, V. Capelle, C. Boonne, N. Poulet-Crovisier, A. Barbe, D. Chris Benner, V. Boudon, L. R. Brown, J. Buldyreva, A. Campargue, L. H. Coudert, V. M. Devi, M. J. Down, B. J. Drouin, A. Fayt, C. Fittschen, J. M. Flaud, R. R. Gamache, J. J. Harrison, C. Hill, Ø. Hodnebrog, S. M. Hu, D. Jacquemart, A. Jolly, E. Jiménez, N. N. Lavrentieva, A. W. Liu, L. Lodi, O. M. Lyulin, S. T. Massie, S. Mikhailenko, H. S. P. Müller, O. V. Naumenko, A. Nikitin, C. J. Nielsen, J. Orphal, V. I. Perevalov, A. Perrin, E. Polovtseva, A. Predoi-Cross, M. Rotger, A. A. Ruth, S. S. Yu, K. Sung, S. A. Tashkun, J. Tennyson, V. G. Tyuterev, J. Vander Auwera, B. A. Voronin and A. Makie, *Journal of Molecular Spectroscopy*, 2016, **327**, 31–72.

55 A. V. Nikitin, O. M. Lyulin, S. N. Mikhailenko, V. I. Perevalov, N. N. Filippov, I. M. Grigoriev, I. Morino, T. Yokota, R. Kumazawa and T. Watanabe, *Journal of Quantitative Spectroscopy and Radiative Transfer*, 2010, **111**, 2211–2224.

56 A. V. Nikitin, O. M. Lyulin, S. N. Mikhailenko, V. I. Perevalov, N. N. Filippov, I. M. Grigoriev, I. Morino, Y. Yoshida and T. Matsunaga, *Journal of Quantitative Spectroscopy and Radiative Transfer*, 2015, **154**, 63–71.

57 A. M. Zolot, F. R. Giorgetta, E. Baumann, W. C. Swann, I. Coddington and N. R. Newbury, *Journal of Quantitative Spectroscopy and Radiative Transfer*, 2013, **118**, 26–39.

58 A.-W. Liu, Y. Tan, C.-L. Hu, J. Wang, Y. R. Sun and S. M. Hu, Poster N9, Book of abstracts, Université Bourgonge Franche-Comté, Dijon-France, 2019.

59 H. Lin, L. Yang, X. J. Feng and J. T. Zhang, *Physical Review Letters*, 2019, **122**, 013002.

60 S. Kassi, B. Gao, D. Romanini and A. Campargue, *Phys. Chem. Chem. Phys.*, 2008, **10**, 4410–4419.

61 B. Gao, S. Kassi and A. Campargue, *Journal of Molecular Spectroscopy*, 2009, **253**, 55–63.

62 L. Wang, S. Kassi and A. Campargue, *Journal of Quantitative Spectroscopy and Radiative Transfer*, 2010, **111**, 1130–1140.

63 A. Campargue, L. Wang, D. Mondelain, S. Kassi, B. Bézard, E. Lellouch, A. Coustenis, C. d. Bergh, M. Hirtzig and P. Drossart, *Icarus*, 2012, **219**, 110–128.

64 A. Campargue, O. Leshchishina, L. Wang, D. Mondelain and S. Kassi, *Journal of Molecular Spectroscopy*, 2013, **291**, 16–22.

65 M. Hirtzig, B. Bézard, E. Lellouch, A. Coustenis, C. de Bergh, P. Drossart, A. Campargue, V. Boudon, V. Tyuterev, P. Rannou, T. Cours, S. Kassi, A. Nikitin, D. Mondelain, S. Rodriguez and

S. Le Mouélic, *Icarus*, 2013, **226**, 470–486.

66 C. de Bergh, R. Courtin, B. Bézard, A. Coustenis, E. Lellouch, M. Hirtzig, P. Rannou, P. Drossart, A. Campargue, S. Kassi, L. Wang, V. Boudon, A. Nikitin and V. Tyuterev, *Planetary and Space Science*, 2012, **61**, 85–98.

67 A. V. Nikitin, X. Thomas, L. Daumont, M. Rey, K. Sung, G. C. Toon, M. A. H. Smith, A. W. Mantz, A. E. Protasevich, S. A. Tashkun and V. G. Tyuterev, *Journal of Quantitative Spectroscopy and Radiative Transfer*, 2018, **219**, 323–332.

68 K. S. K. Suzumura and H. S. H. Sasada, *Japanese Journal of Applied Physics*, 1995, **34**, L1620.

69 H. Sasada, K. Suzumura and C. Ishibashi, *The Journal of Chemical Physics*, 1996, **105**, 9027–9034.

70 K. Suzumura, C. Ishibashi and H. Sasada, *Optics Letters*, 1997, **22**, 1356–1358.

71 A. V. Nikitin, I. S. Chizhmakova, M. Rey, S. A. Tashkun, S. Kassi, D. Mondelain, A. Campargue and V. G. Tyuterev, *Journal of Quantitative Spectroscopy and Radiative Transfer*, 2017, **203**, 341–348.

72 M. Ghysels, D. Mondelain, S. Kassi, A. V. Nikitin, M. Rey and A. Campargue, *Journal of Quantitative Spectroscopy and Radiative Transfer*, 2018, **213**, 169–177.

73 A. V. Nikitin, M. Rey and V. G. Tyuterev, *The Journal of Chemical Physics*, 2016, **145**, 114309.

74 A. V. Nikitin, M. Rey and V. G. Tyuterev, *Journal of Quantitative Spectroscopy and Radiative Transfer*, 2017, **200**, 90–99.